When Infrared Small Target Detection Meets Tensor Ring Decomposition: A Multiscale Morphological Framework

Lizhen Deng, *Member, IEEE,* Jie Song, Guoxia Xu, *Member, IEEE,* Hu Zhu, *Member, IEEE,*

Abstract—Detecting the small targets from heterogeneous background in infrared image is a challenging problem, which has received extensive attention. In this paper, we propose a method in terms of tensor ring decomposition and nonlinear multi-scale morphological top hat transformation for infrared small target detection (ISTD). Firstly, a tensor model with prior knowledge is constructed for extracting the structural features of multiple infrared images. Then, the problem of small target detection is converted into a problem of minimizing tensor rank with tensor ring. Based on the tensor ring decomposition model, we introduce the top-hat regularization into our model with multiple structural elements of different size to perform morphological operations. The corresponding morphological model exploits a more accurate ring top-hat regularization expression through adaptive nonlinear combination for the ISTD problem. Finally, the optimization of the model is realized by the closed solution given by the alternating direction method of multipliers (ADMM) algorithm. In order to verify the superior performance of our method, our method is compared with a number of advanced detection models. By analyzing the results of comparison experiments, the detection accuracy and precision of our model in the detection of small infrared targets have been improved. Even in complex background conditions, our model also maintain a good robustness.

Index Terms—Small Target Detection, Tensor Ring Decomposition, Nonlinear Multi-scale, Ring Top-hat, ADMM.

I. Introduction

INFRARED imaging has the advantages of long imaging distance, strong anti-interference and can be obtained in all-weather and all-day. Therefore, vision technology based on infrared images is widely used in aerospace technology [1], remote sensing [2], [3], medical imaging [4], target detection and tracking [5] and many other fields. As one of the key technologies in the field of computer vision, infrared small target detection technology has received extensive attention and research in recent years. If the imaging system is far away from the target, the target appears as a point target in the infrared image, and there is no distance information. Under this condition, the characteristics such as shape, size and texture, cannot be used to identify the target [6] clearly.

Moreover, the signal-to-noise ratio of infrared image is low, and small targets may be affected by thick clouds or sea-sky level [7], [8], and the point-wise or block-wise targets submerge in the background and noise. Therefore, it is a challenging problem to carry out the detection and tracking of infrared targets under complex background, and it has important theoretical significance and practical value for in-depth research.

Due to the complex environment of infrared imaging, the background of infrared image is complex and disturbed by noise, which make it impossible to directly extract the target from the original infrared image. In order to detect and recognize the target quickly and accurately, the original infrared image must be preprocessed to highlight the salient features of the target and provide convenience for subsequent target detection and recognition. The classic methods are to use prior knowledge of the image background such as median filtering [9], the max-mean/max-median filtering [10] and the top-hat filtering [1]. These methods use traditional methods of background estimation to separate targets, usually using neighborhoods to predict current pixels, and detect small targets by subtracting the original picture and the estimated background. In addition, some methods that use the discontinuity of the target and the surrounding area and have significant features can improve the detection effect, such as the local contrast measure (LCM) [2], the multiscale patch-based contrast measure (MPCM) [11] and local adaptive comparison operation based on regularized feature reconstruction [12]. Pang et al. [13] proposed a novel spatiotemporal saliency method by using the spatial saliency map and temporal saliency map. However, these methods will be interfered by other factors such as strong edges of the image, resulting in a high false alarm rate, that is, high detection errors.

Recently, fuzzy metric methods have been proposed to solve the above problems, such as multi-scale fuzzy metric [14], multi-channel kernel fuzzy correlation map [15] and space-based improved fuzzy mean [16] method. With the development of the top-hat filter [1], matrix completion [6], [17], and tensor completion [18]–[20] and other related technologies, the detection technology has been greatly improved.

Obviously, the image representation and feature extraction play a vital role in the infrared small target detection. With the research and development of low-rank matrices, low-rank matrix has demonstrated their excellent performance and has been used in infrared small target detection technology [6], [17], [21], [22]. Because small targets are often considered
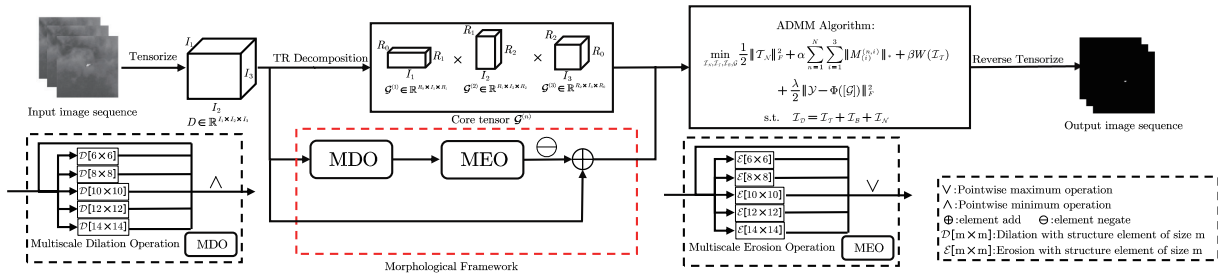
Fig. 1. The detection process of proposed model.

irrelevant to the background and belong to the high-frequency part of the image. The inherent spatial correlation between image pixels indicates that the pixels in the background expressed in a continuous manner are highly correlated. It can be considered that the small target destroys the local correlation of the background. If the target is segmented from the background, the obtained background image can restore this correlation. Then the small target detection problem is transformed into segmenting the target from the background to achieve the restoration of the low-rank matrix of the background. For example, Gao et al. [6] proposed an infrared patch image model (IPM) based on the similarity of local block structure, and described the detection of small infrared targets as an optimization problem of low rank and sparse matrix restoration of the background. Dai et al. [20] generalized IPM to an infrared patch-tensor (IPT) model which uses the prior information of image structure. However, the solution of low-rank matrix is an NP-hard problem. In order to correctly detect small infrared targets in a highly heterogeneous background, He et al. [17] proposed a low-rank sparse representation model under the assumption of multi-subspace clustering. However, nuclear norm minimization (NNM) tends to shrink the rank component excessively.

In recent years, convolutional neural networks combined with classic computer version algorithms have developed rapidly. Inspired by the advantages of deep learning technology in feature extraction and learning, More and more target detection models have been proposed, such as target to clutter ratio convolutional neural network presented by McIntosh et al. [23]. By using the filters of the first convolutional layer are composed of the eigenvectors most responsive to targets or to clutter to optimize a target to clutter ratio metric defined as the ratio of the output energies produced by the network in response to targets and clutter. Kong et al. [24] proposed a model consisting of two winds, Dual-Path Network module and fusion transition module, to conduct efficient target extraction. Wang et al. [25] proposed a new feature extraction back-bone network for small infrared target detection. Dai et al. [26] proposed a model-driven deep network which can make use of both labeled data and the domain knowledge. However contemporary deep learning-based methods have achieved high detection accuracy and real-time speed in many fields, but these methods are highly data driven. The availability of large amounts of training data is essential to robust learn the features. Under certain conditions, it is difficult to obtain massive amounts of marked infrared data which requires a lot of labor costs. Therefore, some classic

methods without training have their unique advantages, such as top-hat transformation and tensor decomposition.

Tensor decomposition has attracted considerable attention in various fields. Some traditional tensor decomposition methods are still widely followed, such as CANDECOMP/PARAFAC((CP) [27]. Xue et al. [28] proposed a new multilayer sparsity-based tensor decomposition by using CP to measure the first-layer sparsity. Other kinds of decompositions such as Trucker, Tensor Train (TT) [29] and Tensor Ring (TR) are shown to reveal the structure in the data with the notion of rank extended to the notion of a multi-rank, expressed as a vector of ranks of the factors in the contracted representation using matrix product states. Bu et al. [30] proposed an image fusion model by using tucker decomposition to fully exploit the intrinsic global spatial-spectral information. Liu et al. [31] established a spatio-temporal tensor model and reduced small target Detection to a low-rank sparse tensor decomposition problem. With the Tucker tensor decomposition method, better detection performance is obtained in complex backgrounds. Zhang et al. [32] improved the above spatio-temporal tensor model by making it enhanced for edge and corner awareness. Pang et al. [33] adopted greedy bilateral factorization strategy for its low computational load to approximate the low-rank term.

In this paper, we consider the use of tensor ring completion to achieve low-rank matrix restoration of infrared images. The key to the completion of the tensor ring is the low-rank hypothesis of the tensor. The methods can be divided into two categories: methods based on tensor decomposition and methods based on rank minimization. Since the optimal rank is usually data dependent, it is very challenging to specify the optimal rank in advance. Therefore, the method based on rank minimization is usually used to minimize the tensor rank using convex algebra. Based on different definitions of tensor rank, various nuclear norm regularized algorithms have been proposed [18], [34], [35] to achieve tensor completion. Overall, these existing methods [21], [36]–[38] are inevitably inheriting the issues from inherent high sensitivity of rank selection and low calculation efficiency. Different with above assumption, in this paper, we adopt the tensor ring (TR) decomposition to solve the ISTD problem, which establishes a theoretical relationship between the rank of the multi-linear tensor and the rank of the TR factor. Thus the low-rank constraint can be implicitly realized on the TR latent space, and then further combine with the kernel norm regularization to obtain a stable solution. Furthermore, the proposed model can also improve by the fast SVD calculation of small size factor. Therefore,

this methodology provides performance stability and high calculation efficiency from mode construction.

In addition, because the noise in the infrared image is regarded as the high-frequency part of the image, it will be mistaken for the target during the model detection process, which reduces the detection accuracy. For example, in the Top-Hat transformation [39], the noise in the infrared image will increase the false alarm rate or false alarm rate and reduce the detection probability, which is not conducive to target detection. Mathematical morphology is the theory and technology of analyzing and processing the geometric structure of images [40]. The model based on morphology can use the geometric feature information of the target in the image to construct the corresponding structural elements, remove the parts that are irrelevant to the structural elements, and retain the coherent parts [41], which can effectively remove noise and retain useful image information. Therefore, in recent years, morphology has been widely used in infrared small target detection, and the top-hat transformation is an important operation in this application [1], [42]–[44], such as a ring-based top-hat operator for small target detection in [42], [45]. However, traditional morphological operators use single-scale structural elements, ignoring the associated information between the target and the surrounding area, and the detection effect is not good if the image signal-to-noise ratio(SNR) is low. In order to find suitable structural elements for target detection, some algorithms based on neural networks and genetic algorithms are proposed [1], [46], [47]. Although these algorithms perform well in some situations, they do not directly improve the top-hat transformation. The multi-scale operation of top hat transformation [48] can directly improve the performance of top hat transformation by changing structural elements to suppress the influence of noise [44].

This paper attempts to start from the perspective of changing structural elements based on morphology [41] and perform morphological operations on the structure elements of different sizes. Intuitively, non-linear combination (point-wise maximum operation) [49] are embedded to achieve the multiscale ring top-hat transformation to improve the detection effect of small targets shown in Fig. 1. Therefore, in order to solve the problem of insufficient background prior knowledge and image noise affecting detection accuracy, we propose a new improved infrared target detection method that combines tensor ring approximation with ring top-hat regularization based on adaptive morphology, termed as TRDSD. We list the main contributions of this article as follows.

- By converting the small target detection problem into a tensor rank minimization problem, the tensor ring is introduced to complete the infrared small target detection. The Properties of tensor ring decomposition can be used to avoid curse of dimensionality, while providing strong and generalized ability. Using tensor ring decomposition in our model can effectively suppress background and enhance detection.
- In order to achieve detail preservation and noise suppression, morphological reconstruction is used to filter the image background, and multiscale morphological reconstruction images based on different structural elements

are non-linearly combined to improve the traditional top-hat regularization and obtain more accurate object detection.
- The tensor ring completion and the adaptive top-hat regularization term are combined to construct the objective function of the model, and the optimization of the model is achieved by ADMM algorithm. The experimental results compared with multiple advanced detection methods confirm that our TRDSD has greatly improved the detection probability and false alarm rate.

The rest of the paper is organized as follows. In Section II, We introduce the theoretical basis of our model and related work. then we introduce in detail our model in Section III. Section IV analyzes the experiments and results of our model and the state-of-the-art algorithms. Finally, a briefly conclusion of our work is given in Section VI.

II. RELATED WORK

A. Tensor Ring Decomposition and Tensor Completion

The notations of tensor in [27] are adopted in this paper. A vector is denoted by a lower case letter, $e.g.$, $t \in \mathbb{R}^I$. A matrix is denoted by a upper case letter, $e.g.,$, $I_D \in \mathbb{R}^{I \times N}$, and a tensor of order N is denoted by a calligraphic letter, $e.g.$, $\mathcal{I}_D \in \mathbb{R}^{I_1 \times I_2 \times \cdots \times I_N}$, then the tensor sequence is $\mathcal{I}_D = i_{d_1}, \cdots, i_{d_n}, \cdots, i_{d_n}$, where $1 \leqslant d_n \leqslant I_n$. The inner product of two tensor $\mathcal{I}_D, \mathcal{I}_B \in \mathbb{R}^{I_1 \times I_2 \times \cdots \times I_N}$ is defined as $< \mathcal{I}_D \cdot \mathcal{I}_B >= \sum_{i_1} \sum_{i_2} \cdots \sum_{i_N} i_{d(i_1 \cdots i_N)} i_{b(i_1 \cdots i_N)}$.

The tensor ring (TR) decomposition is a general decomposition model in tensor research area. The tensor ring is a high-order tensor of the circular multi-linear product on a series of low-order latent core tensors (TR factors). And the TR factors are denoted as $\mathcal{G}^{(n)} \in \mathbb{R}^{R_n \times I_n \times R_{n+1}}$, and each contains three modes, where mode-1 and mode-3 are rank-modes and mode-2 is a dimension-mode, thus all the TR factors can be set in 3-order.

Next we discuss the relationship between TR decomposition and traditional decomposition. tensor-SVD (t-SVD) [50] can only handle third-order tensors, which limits it to handle higher-order tensors. Numerically, for a given rth-order tensor, the space complexity of CANDECOMP/PARAFAC(CP) [27], Tensor Train (TT) [29], and Tensor Ring(TR) [51] decomposition are linear to tensor order, while the number of parameters in Tucker model is $\mathcal{O}\left(dnr + r^d\right)$ that is exponential to tensor order causing the curse of dimensionality. Besides, although the number of parameters in CP decomposition is linear to tensor order, the optimization problem about searching for best latent tensors is not easy. Since TT decomposition has strict condition $R_1 = R_{N+1} = 1$ and relatively fixed pattern, i,e., rank-1 condition on the border factors and larger in middle factors which ends up with restricted representation ability and flexibility. It should be noted that TR decomposition takes use of trace operations and thus the TR decomposition relaxes the rank constraint on the first and last core of TT to $R_1 = R_{N+1}$. Moreover, TR can be considered as a linear combination of TTs for the reason that TR decomposition linearly scales to the order of the tensor and alleviates highly dependence on

permutation of the original tensor. Thus, it can offer a powerful and generalized representation ability.

The element-wise relation of TR decomposition and the generated tensor are given by:

$$\mathcal{I}_{\mathcal{D}}(i_1, i_2, \cdots, i_N) = \text{trace}\{\prod_{n=1}^{N} G_{i_n}^{(n)}\} \qquad (1)$$

where $\text{trace}\{\cdot\}$ is the matrix trace operation, $G_{i_n}^{(n)} \in \mathbb{R}^{R_n \times R_{n+1}}$ denotes the i_n-th mode-2 slice matrix of $\mathcal{G}^{(n)}$, that is, $\mathcal{G}^{(n)}(:, i_n, :)$.

For the formulation of the model, the tensor completion problem is set to weighted least squares (WLS) model. The tensor completion algorithms are different based on different tensor decompositions, and the TRALS [51], TRWOPT [52] and RTRC [53] are both TR-based tensor completion. The optimization model used in above algorithms is formulated as:

$$\min_{[\mathcal{G}]} \|P_\Omega(\mathcal{T} - \Psi([\mathcal{G}]))\|_F^2 \qquad (2)$$

where the optimization objective is the TR factors $[\mathcal{G}]$, $\mathcal{T}$ is the N-dimension incomplete tensor and $P_\Omega(\mathcal{T})$ represents the entries with respect to the set of indices Ω. The $\Psi([\mathcal{G}])$ represents the approximated tensor which is generated by $\mathcal{G}$ and can be calculated by Equ. 2.

B. Ring Top-Hat Transformation

The classical Top-Hat transformation uses two same structuring elements. In this way, it inappropriately considers the differences between the target and surrounding regions. In order to utilize the difference information between the target region and surrounding background, the method of two different ring shape structuring elements in the transformation is proposed.

As shown in Fig. 2, b_i and b_o are two planar structural elements with the same shape and different sizes. Let the size of the structural element b be $S(b)$, that is, the radial distance from the center of b to the contour of b. Then, b_o means a structural element larger than the target area and is called a outer structural element. b_i represents an inner structural element, where $S(b_i) < (b_o)$. Then the margin area between b_i and b_o is the edge structure element $\Delta b = b_o - b_i$. , $S(\Delta b)$ is the radial distance from the center of Δb to the outer contour of ΔB, then $S(\Delta b) = S(b_o)$. Let $M(\Delta b)$ be the radial distance from the inner contour to the outer contour of Δb, then $M(\Delta b) = S(b_o) - S(b_i)$. b_d represents a structural element whose size is between $S(b_o)$ and $S(b_i)$. In Fig. 2, O is the origin of the structuring elements. Then, based on Equ. 3, the opening operation and closing operations of ring top-hat transformation are defined as follows:

$$(f \circ b_{oi})(x, y) = (f \ominus \Delta b) \oplus b_d$$
$$(f \bullet b_{oi})(x, y) = (f \oplus \Delta b) \ominus b_d \qquad (3)$$

where b_{oi} means the operation related to b_o and b_i. Then, the ring top-hat transformation can be defined as follows:

$$RWTH(x, y) = f(x, y) - (f \circ b_{oi})(x, y)$$
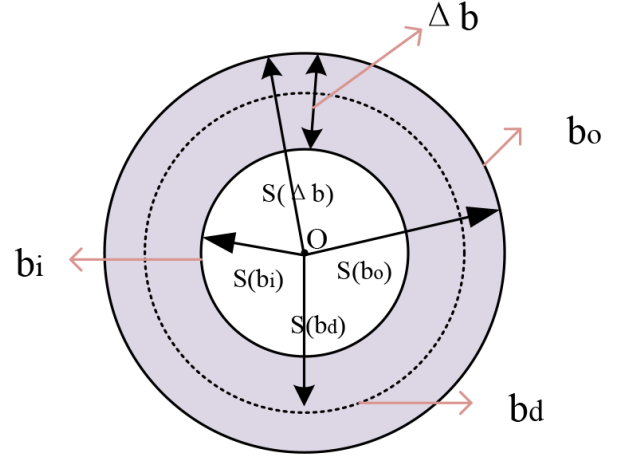$$RBTH(x, y) = (f \bullet b_{oi})(x, y) - f(x, y) \qquad (4)$$

Fig. 2. Relationship of the structuring elements.

III. PROPOSED METHOD FOR SMALL TARGET DETECTION

In this part, we introduce the construction and reasoning of the proposed model. We superimpose multiple frames of infrared images into a tensor as an input image block ($\mathcal{I}_{\mathcal{D}}$). Based on the typical problem of essentially recovering low-rank components and sparse components from the data matrix of traditional small target detection, we improve the target detection task to take the background low-rank and morphological operators as constraints to solve the convex optimization minimization problem of Gaussian noise. In addition, we also introduce the entire model for target detection, namely adaptive ring top-hat and tensor ring decomposition. Finally, the solution process of each part based on ADMM is explained in detail.

A. The Improved Target Detection Task

In order to facilitate the discussion, the matrix form is generally used to represent the image. Therefore, given the original infrared image I_D, it is mainly composed of three parts: target image, background image and noise image, which are represented by I_T, I_B and I_N respectively. The description of small target detection is presented as follows:

$$I_D = I_T + I_B + I_N \qquad (5)$$

To achieve effective and accurate detection of small infrared targets, the model starts from two aspects: (1) Suppress the background I_B and noise I_N of the input image I_D. (2) Use morphological operators to enhance the target I_T. Thus the model can be considered as a minimization problem of Gaussian noise as follows:

$$\min_{\mathcal{I}_{\mathcal{D}}, \mathcal{I}_{\mathcal{T}}} \|\mathcal{I}_{\mathcal{D}} - \mathcal{I}_{\mathcal{T}} - \mathcal{I}_{\mathcal{B}}\|_F^2 \qquad (6)$$

B. Motivations on multiscale morphological transformation

Classical top-hat transformation has been widely used in image processing, which is based on the structural elements such as square and circular. The basic idea is applying a certain structural element to execute the traversal operation

and corresponding calculation in an image. However, the classical top-hat transformation is based on the same structural elements for opening or closing operations, and does not use the difference information between the small target and the background, which may reduce the efficiency of the classical top-hat transformation. Moreover, operations based on the same structural elements cannot distinguish the real target area from the noise or clutter area [40], [54]. Image noise may cause the target to be lost or the number of false alarms to increase, thereby affecting the performance of the classical top-hat transform.

If the difference information between the target and background is directly used to construct the elements, the performance of the top-hat transformation will be significantly improved, that is, the ring top-hat transformation [48]. For image processing using morphological operators, large-scale structural elements can suppress noise, while may also blur image details, and small-scale structural elements can retain image details, while may not suppress noise. In order to compromise the effects of the two, some researchers have proposed multi-scale and adaptive morphological operators to improve the performance of traditional morphological operators. However, most multi-scale morphological operators, such as morphological gradient operator and morphological filter operator [55], [56], average the morphological operation results of all scales as the final output. Some researchers improve the multi-scale morphological operator [57] by introducing weighting coefficients with low efficiency. Moreover, both multi-scale and adaptive morphological operators use linear combinations, which are not suitable for multi-scale morphological operations. Therefore, inspired by [49], we try to use nonlinear combinations (that is, point-to-maximum operations represented by $\vee$) to design adaptive morphological operators. Let b and f represent the structuring element and the image to be processed. The dilation of adaptive ring top-hat operator can be defined as $\delta^{(n)}(f)$, where $\delta^{(1)}(f) = (f \ominus b_1) \wedge f$ and $\delta^{(k)}(f) = (\delta^{(k-1)}(f) \ominus b_k) \wedge \delta^{(k-1)}(f)$, $2 \leq k \leq n$, $k, n \in N^+$, and $\wedge$ stands for the point-wise minimum at each pixel of two images. And the erosion operation of ring top-hat transformation is defined by $\varepsilon^{(n)}(f)$, where $\varepsilon^{(1)}(f) = (f \ominus b_1) \vee f$, $\varepsilon^{(k)}(f) = (\varepsilon^{(k-1)}(f) \ominus b_k) \vee \varepsilon^{(k-1)}(f)$ for $2 \leq k \leq n$, $k, n \in N^+$. Thus the adaptive opening and closing of ring top-hat is obtained as follows.

$$\gamma(f) = \delta^{(n)}(\varepsilon^{(n)}(f))$$
$$\phi(f) = \varepsilon^{(n)}(\delta^{(n)}(f)) \qquad (7)$$

Then the new white top-hat transformation and black top-hat transformation of image f is defined by

$$\omega TH = f - \gamma(f)$$
$$\flat TH = \phi(f) - f \qquad (8)$$

Therefore, the tensor representation of multiple frames of infrared images is constructed in our model, we present a new adaptive ring top-hat operator here:

$$W(\mathcal{I}_\mathcal{T}) = \mathcal{I}_\mathcal{T} - O_S(\mathcal{I}_\mathcal{T}) \qquad (9)$$

C. Tensor decomposition based on tensor ring low-rank kernel

In infrared images, the adjacent pixels of the local background are highly correlated. Assuming that the background transition is slow, the low-rank prior information of the background has high usability. Therefore, the problem of small target detection is transformed into a background low-rank tensor recovery problem. The initial assumption of the low-rank property in background can be described as

$$\text{rank}(I_B) < k \qquad (10)$$

where k is a constant, representing the complexity of the background image. Generally speaking, the value k of the complex background is greater than the value k of the uniform background.

However, rank minimization is an NP-hard problem. Based on the concept of low-rank matrix completion, the tensor rank is defined as the sum of rank in mode-n unfolding of the object tensor [27]. In order to solve the problems of traditional tensor completion methods, we applied a low rank to each TR factor, thus establishing our basic tensor completion model. Then the tensor completion problem can be defined as:

$$\min_{[\mathcal{G}], \mathcal{X}} \sum_{n=1}^N \left\| G_{(2)}^{(n)} \right\|_* + \frac{\lambda}{2} \left\| \mathcal{I}_\mathcal{B} - \Phi([\mathcal{G}]) \right\|_F^2 \qquad (11)$$

where $G_{i_n}^{(n)} \in \mathbb{R}^{R_n \times R_{n+1}}$ denotes the i_n-th mode-2 slice matrix of $\mathcal{G}^{(n)}$.

Completion by TR decomposition The algorithm based on tensor decomposition does not directly use rank constraints on the object tensor, but sets the tensor completion problem to a weighted least squares (WLS) model, and uses the latent factors of tensor decomposition to predict the missing content. The specific expression is as follows:

$$\min_{[\mathcal{G}]} \left\| P_\Omega(\mathcal{I} - \Phi([\mathcal{G}])) \right\|_F^2 \qquad (12)$$

There is a detailed introduction of model functions in related work.

Completion by nuclear norm regularization The nuclear norm defined by $\|I_B\|_* := \sum_k \sigma_k(I_B)$ is a commonly used method at present. The convex algebra of the nuclear norm is applied to the low-rank tensor model, and all the mode-n unfolding simultaneously of the object tensor are regularized. Thus the model of rank minimization-based tensor completion can be formulated as:

$$\min_\mathcal{X} \text{rank}(\mathcal{X}) + \frac{\lambda}{2} \left\| P_\Omega(\mathcal{I} - \mathcal{X}) \right\|_F^2 \qquad (13)$$

where $\text{Rank}(\cdot)$ is a rank regularizer and $\mathcal{X}$ represents a recovered low-rank tensor. The model can find the low-rank structure of the data and approximate the restored tensor.

To solve the issues traditional tensor completion methods, we impose low-rankness on each of the TR factors.

$$\min_{[\mathcal{G}], \mathcal{X}} \sum_{n=1}^N \left\| \mathcal{G}^{(n)} \right\|_* + \frac{\lambda}{2} \left\| \mathcal{I}_\mathcal{B} - \Phi([\mathcal{G}]) \right\|_F^2$$
$$\text{s.t.} \quad P_\Omega(\mathcal{X}) = P_\Omega(\mathcal{I}) \qquad (14)$$

The rank of mode-n unfolding of the tensor $\mathcal{X}$ is upper bounded by the rank of the dimension-mode unfolding of the corresponding core tensor $\mathcal{G}^{(n)}$, which allows us to impose a low-rank constraint on $\mathcal{G}^{(n)}$. By the new surrogate, Equ. 14 can be transformed as:

$$\min_{[\mathcal{G}],\mathcal{X}} \sum_{n=1}^{N} \left\| \mathcal{G}^{(n)}_{(2)} \right\|_* + \frac{\lambda}{2} \left\| \mathcal{I}_{\mathcal{B}} - \Phi([\mathcal{G}]) \right\|_F^2 \quad (15)$$
$$\text{s.t.} \quad P_{\Omega}(\mathcal{X}) = P_{\Omega}(\mathcal{I})$$

D. Proposed Model for Small Target Detection

Here, we introduce the proposed new infrared small target detection model in detail. First, in the absence of noise, Equ.5 is transformed into $\mathcal{I}_{\mathcal{D}} = \mathcal{I}_{\mathcal{T}} + \mathcal{I}_{\mathcal{B}}$, then the minimization problem of the aforementioned model is converted to:

$$\min_{\mathcal{I}_{\mathcal{T}},\mathcal{I}_{\mathcal{B}}} \left\| \mathcal{I}_{\mathcal{D}} - \mathcal{I}_{\mathcal{B}} - \mathcal{I}_{\mathcal{T}} \right\|_F^2 \quad (16)$$

Then, combining Equ. 9 and Equ. 11, the final objective function of the model without noise can be written as follows:

$$\min_{\mathcal{I}_{\mathcal{T}},\mathcal{I}_{\mathcal{B}}} \alpha \sum_{i=1}^{3} u_i \left\| \mathcal{I}_{\mathcal{B}}(i) \right\|_{\omega,s_p}^{\rho} + \beta W(\mathcal{I}_{\mathcal{T}}) \quad (17)$$
$$\text{s.t.} \quad \mathcal{I}_{\mathcal{D}} = \mathcal{I}_{\mathcal{T}} + \mathcal{I}_{\mathcal{B}}$$

where α, β, and rho are constants and u_i is the weight of the i-th dimension.

However, the actual target detection cannot avoid noise interference. Then, to combine with Equ.9 and Equ. 15, the model under gaussian noise assumption can be written as

$$\min_{\mathcal{I}_{\mathcal{N}},\mathcal{I}_{\mathcal{T}},\mathcal{I}_{\mathcal{B}},\mathcal{G}} \frac{1}{2} \left\| \mathcal{I}_{\mathcal{N}} \right\|_F^2 + \alpha \sum_{n=1}^{N} \sum_{i=1}^{3} \left\| M^{(n,i)}_{(i)} \right\|_* + \beta W(\mathcal{I}_{\mathcal{T}})$$
$$+ \frac{\lambda}{2} \left\| \mathcal{Y} - \Phi([\mathcal{G}]) \right\|_F^2$$
$$\text{s.t.} \quad \mathcal{I}_{\mathcal{D}} = \mathcal{I}_{\mathcal{T}} + \mathcal{I}_{\mathcal{B}} + \mathcal{I}_{\mathcal{N}} \quad (18)$$

Then we introduce two Lagrangian variable into Equ. 18 with $\mathcal{I}_{\mathcal{B}} = \mathcal{Y}, M^{(n,i)}_{(i)} = G^{(n)}_{(i)}, n = 1, \cdots, N, i = 1, 2, 3.$, where $[\mathcal{M}] := \mathcal{M}^{(n,i)}{}_{n=1,i=1}^{N,3}$ are the auxiliary variables of $[\mathcal{G}]$. For $n = 1, \cdots, N, i = 1, 2, 3$, $\mathcal{G}^{(n)}, \mathcal{M}^{(n,i)}$ and $\mathcal{Y}^{(n,i)}$ are independent, so we can update them separately.

E. The Optimization of the Proposed Method with ADMM

The optimization of Equ. 18 is solved by introducing the Lagrange multipliers of ADMM algorithm. By introducing equal constraints of auxiliary variables, the augmented Lagrangian function of Equ. 18 in our model can be rewritten as

---

Algorithm 1 ADMM for Solving the Optimization of TRDSD model

1: Step 1. *Input:*
   $\mathcal{I}_{\mathcal{D}}, \mathcal{I}_{\mathcal{Z}} = I,$
2: Step 2. *Initialize:*
   $\mathcal{I}_{\mathcal{B}} = \mathcal{I}_{\mathcal{D}}, \mathcal{Y}_i = \mathcal{I}_{\mathcal{B}}, \mathcal{I}_{\mathcal{N}} = 0, \mathcal{I}_{\mathcal{T}} = 0.$
3: Step 3. *While not converge do:*
   1. Optimize the augmented Lagrangian function Equ. 19 by calculating Equ. 21, Equ. 23, Equ. 26, Equ. 29, Equ. 31 and Equ. 32;
   2. Update the factor $\mathcal{P}^{(n,i)}$ by calculating Equ. 24.
4: Step 4. *Output*

$$L(\mathcal{I}_{\mathcal{N}},\mathcal{I}_{\mathcal{T}},\mathcal{I}_{\mathcal{B}},[\mathcal{G}],[\mathcal{M}],\mathcal{Y}) = \frac{1}{2} \left\| \mathcal{I}_{\mathcal{N}} \right\|_F^2 + \alpha \sum_{n=1}^{N} \sum_{i=1}^{3} \left\| M^{(n,i)}_{(i)} \right\|_*$$
$$+ \beta W(\mathcal{I}_{\mathcal{T}}) + \frac{\lambda}{2} \left\| \mathcal{Y} - \Phi([\mathcal{G}]) \right\|_F^2 - \langle \mathcal{I}_{\mathcal{Z}}, \mathcal{I}_{\mathcal{N}} + \mathcal{I}_{\mathcal{B}} + \mathcal{I}_{\mathcal{T}} - \mathcal{I}_{\mathcal{D}} \rangle$$
$$- \sum_{i=1}^{3} \langle \mathcal{S}_i, \mathcal{I}_{\mathcal{B}} - \mathcal{Y}_i \rangle - \sum_{n=1}^{N} \sum_{i=1}^{3} \langle \mathcal{P}^{(n,i)}, \mathcal{M}^{(n,i)} - \mathcal{G}^{(n)} \rangle$$
$$+ \frac{a}{2} \left\| \mathcal{I}_{\mathcal{N}} + \mathcal{I}_{\mathcal{B}} + \mathcal{I}_{\mathcal{T}} - \mathcal{I}_{\mathcal{D}} \right\|_F^2 + \sum_{i=1}^{3} \frac{p_i}{2} \left\| \mathcal{I}_{\mathcal{B}} - \mathcal{Y}_i \right\|_F^2$$
$$+ \sum_{n=1}^{N} \sum_{i=1}^{3} \frac{u}{2} \left\| \mathcal{M}^{(n,i)} - \mathcal{G}^{(n)} \right\|_F^2 \quad (19)$$

where $\mathcal{I}_{\mathcal{Z}}, \mathcal{S}_i, \mathcal{P}^{(n,i)}$ are Lagrange factors. The entire optimization solution process is shown in Algorithm 1.

1) Update of $\mathcal{G}^{(n)}$: Keep only the part related to $\mathcal{G}^{(n)}$ in Equ. 19 to get the augmented Lagrangian function of $\mathcal{G}^{(n)}$ as

$$L(\mathcal{G}^{(n)}) = \sum_{i=1}^{3} \frac{u}{2} \left\| \mathcal{M}^{(n,i)} - \mathcal{G}^{(n)} + \frac{1}{u} \mathcal{P}^{(n,i)} \right\|_F^2$$
$$+ \frac{\lambda}{2} \left\| \mathcal{Y} - \Phi([\mathcal{G}]) \right\|_F^2 + C_{\mathcal{G}} \quad (20)$$

where $C_{\mathcal{G}}$ is a constant and denotes the other parts of the Lagrangian function, which is irrelevant to updating $\mathcal{G}^{(n)}$. Then $\mathcal{G}^{(n)}$ can be updated by

$$\mathcal{G}^{(n)} = \text{fold}_2((\sum_{i=1}^{3}(uM^{(n,i)}_{(2)} + P^{(n,i)}_{(2)}) + \lambda Y_{\langle n \rangle} G^{(\neq n)}_{\langle 2 \rangle}) \quad (21)$$
$$(\lambda G^{(\neq n),T}_{\langle 2 \rangle} G^{(\neq n)}_{\langle 2 \rangle} + 3uI)^{-1})$$

where $I \in \mathbb{R}^{R_n^2 \times R_n^2}$ is the identity matrix.

2) Update of $\mathcal{M}^{(n,i)}$: According to Equ. 19, the augmented Lagrangian function about $\mathcal{M}^{(n,i)}$ is as follows:

$$L(\mathcal{M}^{(n,i)}) = \frac{u}{2} \left\| \mathcal{M}^{(n,i)} - \mathcal{G}^{(n)} + \frac{1}{u} \mathcal{P}^{(n,i)} \right\|_F^2$$
$$+ \left\| M^{(n,i)}_{(i)} \right\|_* + C_{\mathcal{M}} \quad (22)$$

The closed-form solution is given by

$$\mathcal{M}^{(n,i)} = \text{fold}_i(D_{\frac{1}{u}} \left(G^{(n)}_{(i)} - \frac{\alpha}{u} \mathcal{P}^{(n,i)}_{(i)} \right)) \quad (23)$$

where $D_{\frac{1}{u}}(\cdot)$ is singular value thresholding (SVT) operation. If the singular value decomposition of matrix A is USV^T, then $D_{\frac{1}{u}}(A) = U\hat{S}V^T$, $\hat{S} = \max\{S - \frac{1}{u}I, 0\}$.

3) Update of $\mathcal{P}^{(n,i)}$: The augmented Lagrangian function about $\mathcal{M}^{(n,i)}$ is updated by

$$\mathcal{P}^{(n,i)} = \mathcal{P}^{(n,i)} + u(\mathcal{M}^{(n,i)} - \mathcal{G}^{(n)}) \quad (24)$$

where u denotes the penalty parameter: $u = \max\{\rho u, u_{\max}\}$ for each iteration, and ρ is a tuning hyper parameter ($1 < \rho < 1.5$).

4) Update of $\mathcal{I}_{\mathcal{N}}$: The update function of $\mathcal{I}_{\mathcal{N}}$ is described below

$$L(\mathcal{I}_{\mathcal{N}}) = \frac{1}{2}\|\mathcal{I}_{\mathcal{N}}\|_F^2 + \frac{a}{2}\left\|\mathcal{I}_{\mathcal{N}} + \mathcal{I}_{\mathcal{B}} + \mathcal{I}_{\mathcal{T}} - \mathcal{I}_{\mathcal{D}} - \frac{\mathcal{I}_{\mathcal{Z}}}{a}\right\|_F^2 + C_{\mathcal{I}_{\mathcal{N}}} \quad (25)$$

then the solution of $\mathcal{I}_{\mathcal{N}}$ is given as

$$\mathcal{I}_{\mathcal{N}} = \frac{1}{a+1}(\mathcal{I}_{\mathcal{Z}} - a(\mathcal{I}_{\mathcal{B}} + \mathcal{I}_{\mathcal{T}} - \mathcal{I}_{\mathcal{D}})) \quad (26)$$

5) Update of $\mathcal{I}_{\mathcal{T}}$: The solution of $\mathcal{I}_{\mathcal{T}}$ is described below

$$L(\mathcal{I}_{\mathcal{T}}) = \beta W(\mathcal{I}_{\mathcal{T}}) + \frac{a}{2}\left\|\mathcal{I}_{\mathcal{N}} + \mathcal{I}_{\mathcal{B}} + \mathcal{I}_{\mathcal{T}} - \mathcal{I}_{\mathcal{D}} - \frac{\mathcal{I}_{\mathcal{Z}}}{a}\right\|_F^2 + C_{\mathcal{I}_{\mathcal{T}}} \quad (27)$$

According to [58], the optimal solution of Equ. 27 is presented in the model, and the corresponding sub-gradient can be obtained instead of the gradient because of its concave property.

$$\beta\left(\frac{\delta}{\delta(\mathcal{I}_{\mathcal{T}})}W(\mathcal{I}_{\mathcal{T}})\right) + a\left(\mathcal{I}_{\mathcal{N}} + \mathcal{I}_{\mathcal{B}} + \mathcal{I}_{\mathcal{T}} - \mathcal{I}_{\mathcal{D}} - \frac{\mathcal{I}_{\mathcal{Z}}}{a}\right) = 0 \quad (28)$$

Then the updating for corresponding iteration is given as

$$\mathcal{I}_{\mathcal{T}}^{(n+1)} = \mathcal{I}_{\mathcal{D}}^{(n+1)} + \frac{\mathcal{I}_{\mathcal{Z}}}{a} - \mathcal{I}_{\mathcal{N}}^{(n+1)} \\ - \mathcal{I}_{\mathcal{B}}^{(n+1)} - \frac{\beta}{a}\left(\frac{\delta}{\delta(\mathcal{I}_{\mathcal{T}})}W(\mathcal{I}_{\mathcal{T}})\right)_{\mathcal{I}_{\mathcal{T}}^{(n)}} \quad (29)$$

6) Update of $\mathcal{I}_{\mathcal{B}}$: The update function of $\mathcal{I}_{\mathcal{B}}$ is described below

$$\min_{\mathcal{I}_{\mathcal{B}}}\left\{\frac{a}{2}\left\|\mathcal{I}_{\mathcal{N}} + \mathcal{I}_{\mathcal{B}} + \mathcal{I}_{\mathcal{T}} - \mathcal{I}_{\mathcal{D}} - \frac{\mathcal{I}_{\mathcal{Z}}}{a}\right\|_F^2 \\ + \sum_{i=1}^{3}\frac{\rho_i}{2}\left\|\mathcal{I}_{\mathcal{B}} - \mathcal{Y}_i - \frac{\mathcal{S}_i}{\rho_i}\right\|_F^2\right\} \quad (30)$$

then the solution of updating $\mathcal{I}_{\mathcal{B}}$ is given as

$$\mathcal{I}_{\mathcal{B}} = \frac{a(\mathcal{I}_{\mathcal{D}} - \mathcal{I}_{\mathcal{N}} - \mathcal{I}_{\mathcal{T}}) + \mathcal{I}_{\mathcal{Z}} + \sum_{i=1}^{3}(\rho_i\mathcal{Y}_i + \mathcal{S}_i)}{a + \rho_1 + \rho_2 + \rho_3} \quad (31)$$

7) Update of $\mathcal{Y}$:

$$L(\mathcal{Y}) = \frac{\lambda}{2}\|\mathcal{Y} - \Phi([\mathcal{G}])\|_F^2 + \frac{p}{2}\left\|\mathcal{Y} - (\mathcal{I}_{\mathcal{B}} - \frac{\mathcal{S}}{p})\right\|_F^2 + C_{\mathcal{Y}} \quad (32)$$

which is equivalent to the tensor decomposition in Equ. 12.

F. Complexity and Convergence Analysis

In the target recognition task, the given picture sequence is $\mathcal{X} \in \mathbb{R}^{I_1 \times I_2 \times I_3}$, the size of the picture is $I_1 \times I_2$. The size in mode-3 unfolding matric of corresponding TR factors is $m \times n$, where $n = I_1 \times I_2$, $m = I_3$. According to the previous algorithm details, the calculation content of the algorithm is mainly composed of the optimization of adaptive ring top-hat and the parameter update of Tensor Ring Decomposition. For the first part, the dilate operation is computed in $\mathcal{O}(m \times n)$, and therefore, the computing complexity of adaptive ring open operation is $\mathcal{O}(p(m^2 \times n^2))$, where p denotes the number of different structure elements. And for the updating of parameters in TR decomposition, the complexity of updatin $\mathcal{M}$ based on SVD is $\mathcal{O}(\sum_{n=1}^{N} 2I_n R^3 + I_n^2 R^2)$, where $R_1 = R_2 = \cdots = R_N = R$. The complexity of calculating $G_{<2>}^{\neq n}$ is $\mathcal{O}(NR^3 \prod_{i=1,i\neq n}^{N} I_i)$, where N is the iteration number. And the complexity of updating $\mathcal{G}$ is $\mathcal{O}(NR^3 \prod_{i=1}^{N} I_i + NR^6)$. N is set to 3, then overall complexity of our proposed algorithm can be written as $\mathcal{O}(3R^2 I_1 \times I_2 \times I_3 + 3R^6)$. Based on the earlier analysis, the computational complexity of our model is around $\mathcal{O}(3R^2 I_1 \times I_2 \times I_3 + 3R^6 + pI_1^2 \times I_2^2 \times I_3^2)$.
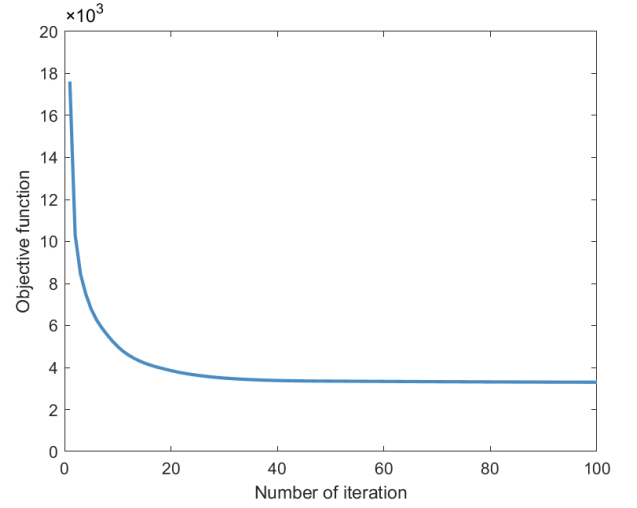

Fig. 3. The convergence chain diagram of TRDSD model.

To prove the convergence of the model, we performed an empirical test in sequence 1. We selected five sets of images for one hundred iterations and recorded the objective function values at each iteration.As shown in Fig. 3, the abscissa of the line graph represents the number of iterations, and the ordinate represents the average result value of the objective function. After many iterations, the value of the objective function tends to be stable, indicating that our method can finally find an optimal solution. Moreover, the number of iterations of the objective function approaching the optimal value is not very large, which proves that the convergence of our model is very good.

IV. EXPERIMENTS AND RESULTS

In this part, we first introduce in detail the evaluation indicators of the experiment and the baseline methods for

comparison. Then, through the parameter setting and adjustment, the influence of the parameters and real image sequence information on the detection effect of our model is discussed. Finally, we conduct comparative experiments based on real image sequences, and highlight the superiority of TRDSD model by analyzing the index data of the charts and figures. In addition, all our experiments are implemented in MATLAB R2018a on a laptop with Intel Core i7-8550U CPU and 8-GB RAM environment.

A. Evaluation Metrics and Baseline Methods

Evaluation Metrics: In the experiments in this paper, the detection probability and false alarm rate are used as indicators to measure the performance of the detection model, which are also the most important indicators to quantify the performance of the current small target detection method. The detection probability represents the probability that the detected target is a true target, and the false alarm rate represents the probability that the detected target is a false target. Their definitions are as follows:

$$P_d = \frac{\text{number of true targets detected}}{\text{number of actual targets}}$$
$$P_f = \frac{\text{number of false detections}}{\text{number of tested frames}} \tag{33}$$

To determine whether an object will be determined as a target by the detection model, two requirements need to be met Simultaneously: 1) The real target and the detection result have overlapping pixels; 2) The distance between the actual target center and the detection result center pixel does not exceed five pixels.

In addition, the experimental analysis also used two common indicators of small target detection performance, namely signal-to-noise ratio gain (SCRG) and background suppression factor (BSF) to show the effects of small target enhancement and background suppression in our detection model. Signal-to-noise ratio (SCR) can be used to describe the difficulty of small target detection. Generally speaking, the higher the SCR of a small target, the easier it is to be detected. Therefore, small target enhancement and background suppression can help improve the accuracy of target detection.

Baseline Methods:

In order to prove the superior performance of the proposed method, the TRDSD was compared with several different methods, and the experimental data was analyzed. The specific baseline methods are:

- Infrared Patch-Image Model (IPI) [59]: The IPI model uses the linear correlation of the local patch structure to transform the small target detection task into an optimization problem of the low-rank sparse matrix that restores the background patch image.
- The model is based on Local Intensity and Gradient Properties (LIG) [60]: The LIG model calculates the local intensity and gradient (LIG) map from the original infrared image to enhance the target and suppress clutter, so as to segment the target well.
- The method is based on non-convex rank approximation minimization joint $\ell_{2,1}$ norm (NRAM) [37]: NRAM

model introduces the structure $\ell_{2,1}$ to wipe out the strong residuals caused by the defects of the nuclear norm and ℓ_1 norm in IPI model.
- The model is based on Partial Sum of the Tensor Nuclear Norm (PSTNN) [61]: PSTNN can efficiently suppress the background and preserve the target and use a local prior map encoded with target-related and background-related information.
- Infrared Small Target Detection via Low-Rank Tensor Completion With Top-Hat Regularization: TCTHR [62]: TCTHR takes both the structural prior knowledge of the target and the self-correlation of the background into account based on low-rank tensor completion with top-hat regularization.
- The model is based on Variance Difference (VARDIIFF) [63]: The method with a three-layer patch-image model can enhance the image of targets and improve the contrast between the target and background, so that the targets can be detected from IR images with a minimum rate of false alarm.

B. Parameters Setting and Data Sets

In the infrared small target detection, the parameter setting also has a great influence on the detection effect, such as the sharp of the structuring element and so on. In order to reflect the effect of parameters on our model, here we mainly analyze the detection indicators of our model in seven real image sequences under different low-rank r of tensors, and give the best parameter configuration. We introduced the information of these seven real image series in detail, and compared the 3D images of different methods on each sequence.

Parameter Setting: Here, we introduce the basic parameter settings of the experiment. In the optimization section of the proposed method above, we set the values of λ, α, and β to 5, 1, and 0.4, respectively. For the structural elements of ring top-hat in Fig. 2, TCTHR [62] model uses the smaller $S(\Delta b)$ and the larger $S(b_d)$ when fixing $S(b_o)$, thus set $S(b_d) = S(b_o)$, and make the values of $S(b_o)$ and $S(b_i)$ as close as possible. This setting is also continued in our model. In addition, since our model adds an adaptive non-linear combination on the basis of the ring top-hat, the model is not sensitive to the value of $S(b_o)$ of the top-hat.

We set the size of the outer ring elements $S(b_o)$, i.e. the image patch size, to 3,5,7,9,11 and combined them non-linearly to suit the task of detecting small targets of different sizes. Each pixel should be manipulated by ring top-hat, i.e. the sliding step size should be 1, in order to keep the image size constant after the operation.

Therefore, we compared our adaptive top-hat regularization with classic top-hat and ring top-hat regularization under the same parameter settings. Based on the three, we take the average of SCRG and BSF in the experimental results to compare and analyze. The specific values are shown in Table I. It can be seen from Table I that the BSF results based on the adaptive ring top-hat are the best results in the 7 image sequences, indicating that the adaptive nonlinear combination can indeed strengthen the suppression of background clutter,

TABLE I
Comparison through Different Top-Hat Regularization

	classical top-hat		ring top-hat		adaptive ring top-hat	
	SCRG	BSF	SCRG	BSF	SCRG	BSF
seq1	22.45	23.30	31.33	34.57	35.27	39.30
seq2	18.00	20.04	24.39	33.89	23.0	34.30
seq3	4.94	4.96	5.52	5.59	5.85	5.97
seq4	11.01	12.30	13.87	16.30	17.61	22.37
seq5	9.78	10.30	10.46	11.09	12.86	14.07
seq6	5.23	5.34	8.87	10.08	9.05	11.97
seq7	5.81	6.07	6.10	6.77	5.95	7.54

thereby improving the robustness of target detection. The result of adaptive ring top-hat regularization is much better than classic top-hat regularization. Moreover, except for seq2 and seq7, our model based on adaptive ring top-hat also obtains the best results of SCRG in the other 5 image sequences, proving that the adaptive ring top-hat regularization improves the detection performance of the ring top-hat to a great extent.

Our model uses tensor decomposition to recover the background low-rank tensor, which is more robust. However, the selection of TR-rank has a considerable influence on the model detection effect. Therefore, we have selected different TR-ranks for experiments respectively, where $r = 2, 4, 6, 8, 10, 12$, and the results of the experiment are shown in Table II, and the best results are marked in red. In seq1, the values of SCRG and BSF are the highest at $r = 2$, and the detection results become worse as the value of r increases. However, in several other sequences, the value of SCRG and BSF changes in a parabolic shape with the increase of r. The optimal results are concentrated under the conditions of $r = 6$ and $r = 8$. And four sequences obtain the optimal value at $r = 8$. Therefore, TR-rank is set to $r = 8$ in subsequent experiments. The experimental results show that such a setting can get a sufficiently good detection effect, and the calculation amount of the model does not increase much. Therefore, imposing a low-rank assumption on the TR factor can bring robustness to the rank selection and alleviate the model selection problem in the experiment to a large extent.

Data Sets: In order to visualize the test data, we randomly select a frame of images from the seven real image sequences, and give the corresponding 3D gray distributions, as shown in Fig. 4. In order to improve the applicability of the model, we use seven real image sequences to simulate as much as possible the diversity of targets and the complexity of the background in the real environment. Specifically, in seq1 of Fig. 4(a), the target is a slow-moving airplane with a sky covered by a large number of clouds in the background. In seq2, the target is far away, it is a ship on the far sea level, and the background is connected by sea and sky. In seq3, the target is a fast-moving airplane, the shape of the airplane is irregular, and the background sky contains thin clouds which are easy to change. In seq4, the image also shows a moving irregular ship in the background of the sea and sky. Unlike the images of seq2, the shooting angle of the camera in seq4 is not parallel to the horizontal plane. And in seq5, the target is a moving, regular-shaped helicopter in a heavily colored sky. Compared

with seq2 and seq4, the target in seq6 and seq7 is closer to the camera. But the background of Seq6 has a background with red and blurred sea and sky. In seq7, the shape of the target is irregular, and the background is a sea surface with water waves. The background of all images includes the sea surface, and the ripples on the sea surface will affect the target detection of the model. In addition, we also give the detection results of our model for the seven original images, as shown in the third row of Fig. 4. Comparing the target position of sub-images in the first row and the detection position of sub-images in the third row in Fig. 4, It can be seen that our model accurately detects the target in the images.

In order to better evaluate our proposed method, we compared the 3D maps of different models to the 7 real sequences in Fig. 4. The specific results are shown in Fig. 5. As shown in Fig. 5, each row from top to bottom represents the results of IPI [59], LIG [60], NRAM [37], PSTNN [61], TCTHR [62], VARDIFF [63] and our TRSDS, respectively. It can be seen from the last row of Fig. 5 that in the 3D maps of the target obtained by our proposed method, the target area is very prominent, and the background near the target is well suppressed. In the first row of Fig. 5, IPI can show the location of the target, however there are other crests that affect the detection, which will increase the false alarm rate of the detection model. In the second row of Fig. 5, the target area in the 3D maps obtained by the LIG method is not significant, and there are many clutters, which makes it difficult to distinguish the target position, so that the performance of LIG method is not ideal.

C. Results on Real Images

To evaluate the superiority of TRDSD method, extensive experiments are implemented in this section. We mainly compared and analyzed the indicators(SCRG and BSF) of different models. Then, the P_d and P_f obtained by TRDSD in each image sequence are compared, and ROC plot and AUC plot on different sequences are given.

For consecutive frames of images randomly selected from seven real infrared image sequences, Table III lists the average values of BSF and SCRG of all models, and the best results are marked in red. It can be seen from Table III that our method does not show obvious advantages in SCRG. Like NRAM and TCTHR, TRDSD only achieved the best results of SCRG indicators in two image sequences. Then for the BSF indicator which reflects background suppression, TRDSD achieved the best results in all image sequences except seq5. And even on seq5, our BSF value is very close to that of the first LIG model. In general, our method can significantly highlight the target, and suppress the background better, which can improve the accuracy of small target detection. Therefore, our method has better detection performance than other baseline methods.

In addition, in order to better compare the detection effect of the model, we calculated the values of P_d and P_f of detection obtained from early image. The specific results are listed in Table IV. Similarly, the optimal values of P_d and P_f are marked in red. It is obvious from Table IV that our model performs much better than other baseline methods. Except for

TABLE II
Values of SCRG and BSF based on different values of TR-rank

	r = 2		r = 4		r = 6		r = 8		r = 10		r = 12	
	SCRG	BSF	SCRG	BSF	SCRG	BSF	SCRG	BSF	SCRG	BSF	SCRG	BSF
seq1	40.35	46.03	38.87	42.65	35.57	39.85	35.27	39.30	29.63	32.7	26.52	28.92
seq2	19.86	26.54	21.74	31.08	22.75	33.25	23.04	34.30	20.37	28.90	16.06	19.07
seq3	5.60	5.71	5.73	5.84	5.87	5.99	5.85	5.97	5.78	5.90	5.55	5.67
seq4	8.01	8.52	12.62	14.47	15.86	19.23	17.61	22.37	17.32	22.33	16.28	20.06
seq5	11.98	12.96	12.76	13.95	13.02	14.27	12.86	14.07	12.03	13.02	1.55	12.40
seq6	8.01	9.83	9.02	11.95	9.05	11.96	9.05	11.97	8.76	11.34	8.46	10.72
seq7	5.71	7.09	5.78	7.23	5.87	7.37	5.95	7.54	5.52	6.76	5.41	6.61

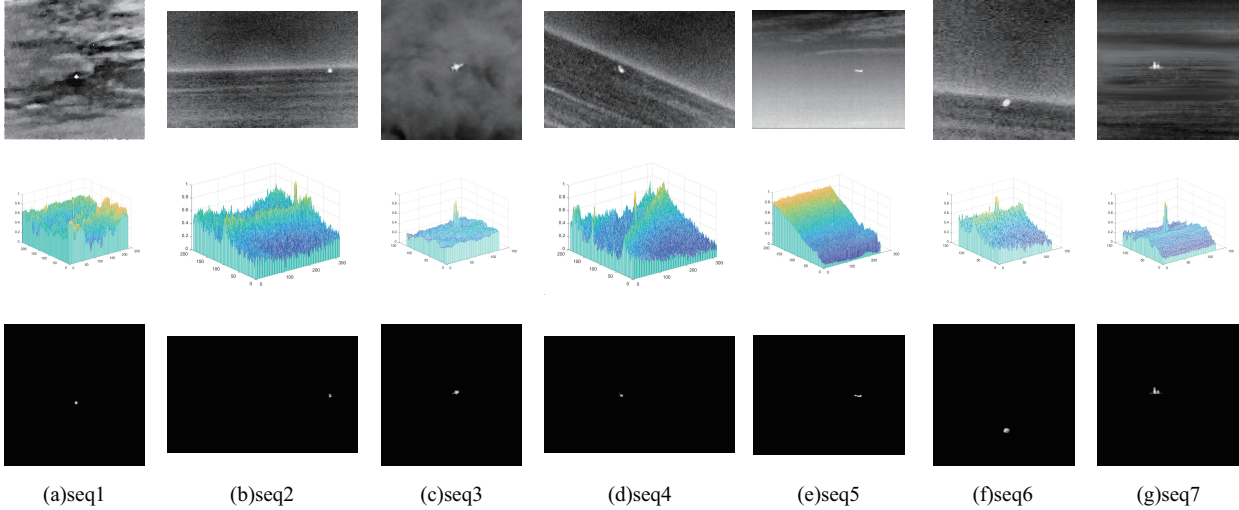(a)seq1 (b)seq2 (c)seq3 (d)seq4 (e)seq5 (f)seq6 (g)seq7

Fig. 4. 7 real infrared image sequences. The sub-images in the first row represent the original images randomly selected from these seven sequences, the second row represents the corresponding 3D gary distribution, and the third row represents the detection results of these seven real images by the TRDSD model.

TABLE III
Values of SCRG and BSF of different methods

	NRAM [37]		IPI [59]		LIG [60]		PSTNN [61]		VARDIFF [63]		TCTHR [62]		TRDSD (ours)	
	SCRG	BSF	SCRG	BSF	SCRG	BSF	SCRG	BSF	SCRG	BSF	SCRG	BSF	SCRG	BSF
seq1	40.75	32.60	13.88	13.54	6.78	7.60	39.01	31.34	17.22	15.13	19.91	20.5	35.27	39.30
seq2	19.68	17.34	8.57	8.29	5.89	9.53	9.29	9.01	14.17	12.77	28.90	29.35	23.04	34.30
seq3	4.48	4.08	3.75	3.73	4.15	5.63	4.63	4.14	4.32	4.10	5.03	5.10	5.85	5.97
seq4	26.52	18.99	6.57	6.48	5.08	6.82	5.26	5.02	9.31	8.52	13.67	14.83	17.61	22.37
seq5	10.28	9.96	8.63	8.46	9.47	14.24	9.48	9.18	10.04	9.41	12.45	12.97	12.86	14.07
seq6	9.70	8.36	3.74	3.61	3.42	6.24	6.14	5.88	6.60	5.95	10.35	10.42	9.05	11.97
seq7	4.80	4.09	3.16	3.07	3.17	6.67	6.02	5.64	4.16	3.86	3.85	5.51	5.95	7.54

TABLE IV
Values of P_d and P_f of different methods

|	NRAM [37]		IPI [59]		LIG [60]		PSTNN [61]		VARDIFF [63]		TCTHR [62]		TRDSD (ours)	
	P_d	P_f	P_d	P_f	P_d	P_f	P_d	P_f	P_d	P_f	P_d	P_f	P_d	P_f
seq1	0.676	0.312	0.645	0.339	0.757	0.248	0.676	0.290	0.879	0.134	0.890	0.108	0,945	0.036
seq2	0.922	0.074	0.735	0.268	0.731	0.235	0.560	0.406	0.864	0.121	0.902	0.070	0.951	0.042
seq3	0.888	0.113	0.897	0.106	0.724	0.237	0.881	0.108	0.969	0.025	0.956	0.033	0.973	0.035
seq4	0.867	0.147	0.791	0.196	0.842	0.159	0.670	0.311	0.761	0.226	0.959	0.043	0.951	0.041
seq5	0.911	0.088	0.857	0.122	0.875	0.105	0.839	0.161	0.923	0.068	0.966	0.026	0.974	0.018
seq6	0.768	.235	0.867	0.111	0.885	0.087	0.895	0.077	0.853	0.119	0.924	0.073	0.969	0.030
seq7	0.699	0.269	0.841	0.131	0.788	0.185	0.867	0.115	0.717	0.246	0.937	0.046	0.956	0.038
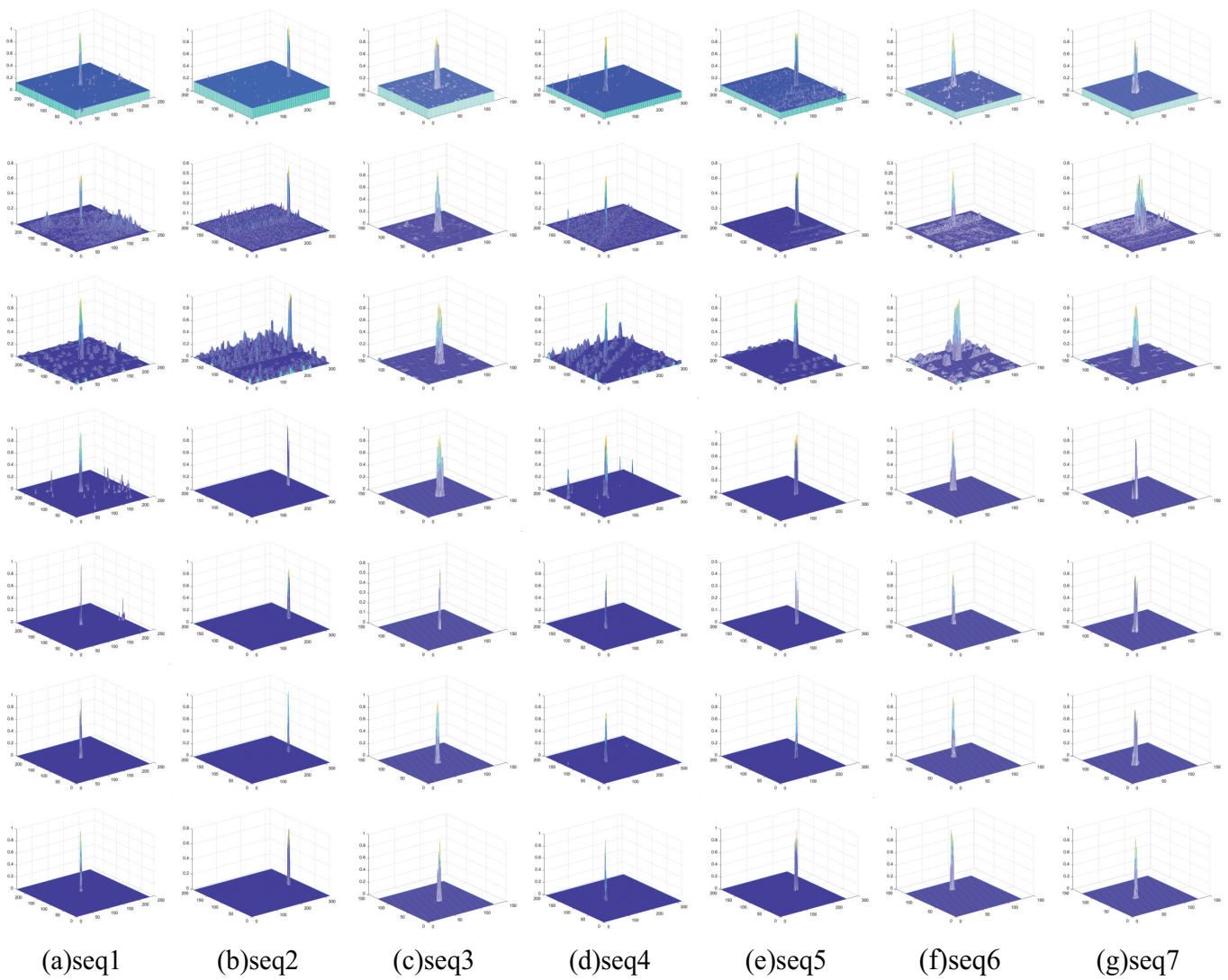
Fig. 5. 3D maps of enhanced results obtained through different baseline methods. Each row from top to bottom represents the results of IPI, LIG, NRAM, PSTNN, TCTHR, VARDIFF and our TRSDS, respectively
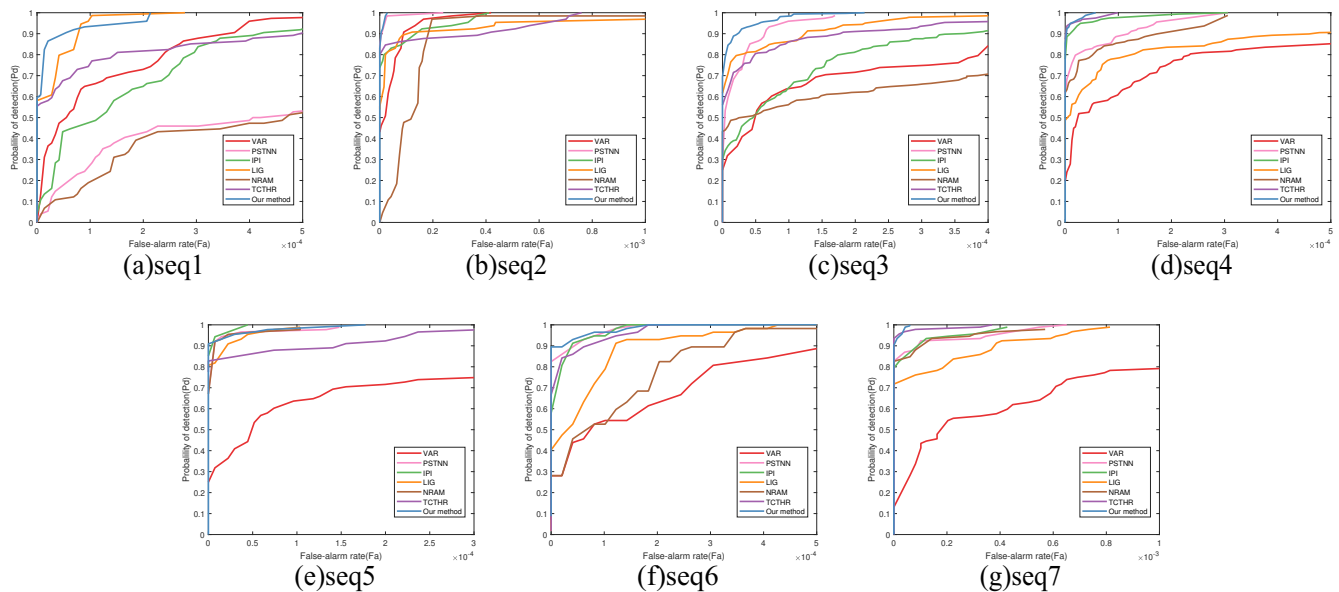

Fig. 6. ROC curves of TRDSD model and the baseline methods on seven real image sequences.

TABLE V
Values of AUC of different methods

	LIG	IPI	NRAM	PSTNN	VARDIFF	TCTHR	TRDSD
seq1	0.63895	0.83431	0.51005	0.83493	0.85645	0.99472	0.99660
seq2	0.95126	0.97174	0.87110	0.97563	0.98917	0.99161	0.99996
seq3	0.98846	0.84257	0.58045	0.66402	0.82207	0.96864	0.97040
seq4	0.95890	0.80049	0.59523	0.94011	0.96601	0.96544	0.99329
seq5	0.98997	0.78381	0.55540	0.78369	076018	0.96268	0.96589
seq6	0.74839	0.86212	0.66129	0.85684	0.89353	0.99022	0.98180
seq7	0.87016	0.92972	0.57228	0.96310	0.92175	0.97984	0.99782

Seq4, TRDSD has the highest value of P_d and is much higher than that of the model on the second place. For example, in seq1, P_d of TRDSD is 6.18% higher than that of TCTHR on the second place. In seq2, TRDSD's P_d is also 3.15% higher than LIG's P_d. Although in seq4, TCTHR model ranks first, our TRDSD is only 0.83% lower than TCTHR, ranking second. Similarly, the false alarm rate of our model has good results. Except for seq3, the false alarm rate of TRDSD is below 0.05, which is much lower than that of other baseline models, and some are even less than half of the P_f of TCTHR, such as in seq1 and seq6. The results prove that the adaptive ring top-hat can strengthen the suppression of background and improve the accuracy of target detection.

In order to understand the superiority of the detection separator of our model, we take the detection probability P_d as the ordinate and false alarm rate P_f as the abscissa to draw the ROC curves of all models on seven image sequences, as shown in Fig. 6. The ROC curve of our TRDSD model is closer to the upper left corner than other models, especially on seq1 and seq2. Therefore, It is believable that the performance of the TRDSD model is better. Table V proves the above point with more specific data. The value of AUC represents the area covered by the ROC curve. The larger the AUC value, the better the classification effect of the classifier, that is, the better the detection model. It can be seen from the table V that our model has obtained the largest AUC values on all four sequences, and the AUC values of our model on seq1, seq2 and seq7 all exceed 0.995, indicating that the detection performance is excellent. In the seq5 and seq6 sequences, our model also ranked second palce, maintaining a fairly good level. Overall, the detection performance of TRDSD is superior to that of TCTHR model.

V. CONCLUSION

This paper proposes an improved infrared small target detection method. The model uses a tensor model constructed with high-dimensional structural features to convert the small target detection problem into a tensor low-rank restoration of the background image. By combining the tensor ring and the adaptive ring top-hat regularization term, our model can suppress the influence of background and noise to achieve better detection results. A large number of experimental results also prove that the detection performance of our model has been improved.

Although tensor ring decomposition based on latent space is not computationally intensive, multiple Ring top-hat operations on each element increase the runtime significantly. In the future, a fast version of the method will be sought to avoid multiple operations on each element.

REFERENCES

[1] M. Zeng, J. Li, and Z. Peng, "The design of top-hat morphological filter and application to infrared target detection," *Infrared Physics and Technology*, vol. 48, no. 1, pp. 67–76, 2006.
[2] C. L. Chen, H. Li, Y. Wei, T. Xia, and Y. Tang, "A local contrast method for small infrared target detection," *IEEE Transactions on Geoence and Remote Sensing*, vol. 52, no. 1, pp. 574–581, 2013.
[3] X. Wang, L. T.Yang, H. Li, M. Lin, and B. Apduhan, "Nqa: A nested anti-collision algorithm for rfid systems," *ACM Transactions on Embedded Computing Systems*, vol. 18, no. 4, pp. 1–21, 2019.
[4] M. Malanowski and K. Kulpa, "Detection of moving targets with continuous-wave noise radar: Theory and measurements," *IEEE Transactions on Geoscience and Remote Sensing*, vol. 50, no. 9, pp. 3502–3509, 2012.
[5] S. Kim and J. Lee, "Scale invariant small target detection by optimizing signal-to-clutter ratio in heterogeneous background for infrared search and track," *Pattern Recognition*, vol. 45, no. 1, pp. 393–406, 2012.
[6] C. Gao, D. Meng, Y. Yang, Y. Wang, X. Zhou, and A. G. Hauptmann, "Infrared patch-image model for small target detection in a single image," *IEEE Transactions on Image Processing*, vol. 22, no. 12, pp. 4996–5009, 2013.
[7] L. Deng, H. Zhu, C. Tao, and Y. Wei, "Infrared moving point target detection based on spatial–temporal local contrast filter," *Infrared Physics and Technology*, vol. 76, pp. 168–173, 2016.
[8] H. Zhu, Y. Guan, L. Deng, Y. Li, and Y. Li, "Infrared moving point target detection based on an anisotropic spatial-temporal fourth-order diffusion filter," *Computers and Electrical Engineering*, vol. 68, pp. 550–556, 2018.
[9] J. T. Barnett, "Statistical analysis of median subtraction filtering with application to point target detection in infrared backgrounds," *Proceedings of SPIE -The International Society for Optical Engineering*, vol. 1050, pp. 10–15, 1989.
[10] S. D. Deshpand, M. Er, V. Ronda, and P. Chan, "Max-mean and max-median filters for detection of small-targets," *Proceedings of SPIE - The International Society for Optical Engineering*, vol. 3809, 1999.
[11] Y. Wei, X. You, and H. Li, "Multiscale patch-based contrast measure for small infrared target detection," *Pattern Recognition*, vol. 58, pp. 216–226, 2016.
[12] Y. Li, Y. Zhang, J. Yu, Y. Tan, J. Tian, and J. Ma, "A novel spatio-temporal saliency approach for robust dim moving target detection from airborne infrared image sequences," *Information Sciences*, p. S00200255516305230, 2016.
[13] D. Pang, T. Shan, P. Ma, W. Li, S. Liu, and R. Tao, "A novel spatiotemporal saliency method for low-altitude slow small infrared target detection," *IEEE Geoscience and Remote Sensing Letters*, pp. 1–5, 2021.
[14] X. Zhou, H. Deng, and X. Sun, "A multiscale fuzzy metric for detecting small infrared targets against chaotic cloudy/sea-sky backgrounds," *IEEE Transactions on Cybernetics*, 2019.
[15] P. Chiranjeevi and S. Sengupta, "Detection of moving objects using multi-channel kernel fuzzy correlogram based background subtraction," *IEEE Transactions on Cybernetics*, vol. 44, no. 6, pp. 870–881, 2014.
[16] X. Bai, Z. Chen, Y. Zhang, Z. Liu, and Y. Lu, "Infrared ship target segmentation based on spatial information improved fcm," *IEEE Transactions on Cybernetics*, vol. 46, no. 12, pp. 3259–3271, 2016.
[17] Y. He, M. Li, J. Zhang, and Q. An, "Small infrared target detection based on low-rank and sparse representation," *Infrared Physics and Technology*, vol. 68, pp. 98–109, 2015.

[18] J. Liu, P. Musialski, P. Wonka, and J. Ye, "Tensor completion for estimating missing values in visual data," *IEEE Transactions on Pattern Analysis and Machine Intelligence*, vol. 35, no. 1, pp. 208–220, 2013.

[19] N. P. Ho, D. T. Hoang, A. B. Johann, and N. D. Minh, "Efficient tensor completion: Low-rank tensor train," *CoRR*, vol. abs/1601.01083, 2016. [Online]. Available: http://arxiv.org/abs/1601.01083

[20] Yimian, Dai, Yiquan, and Wu, "Reweighted infrared patch-tensor model with both nonlocal and local priors for single-frame small target detection," *IEEE Journal of Selected Topics in Applied Earth Observations and Remote Sensing*, vol. 10, no. 8, pp. 3752–3767, 2017.

[21] H. Zhu, H. Ni, S. Liu, G. Xu, and L. Deng, "Tnlrs: Target-aware non-local low-rank modeling with saliency filtering regularization for infrared small target detection," *IEEE Transactions on Image Processing*, vol. PP, 2020.

[22] X. Kong, C. Yang, S. Cao, C. Li, and Z. Peng, "Infrared small target detection via nonconvex tensor fibered rank approximation," *IEEE Transactions on Geoscience and Remote Sensing*.

[23] B. McIntosh, S. Venkataramanan, and A. Mahalanobis, "Infrared target detection in cluttered environments by maximization of a target to clutter ratio (tcr) metric using a convolutional neural network," *IEEE Transactions on Aerospace and Electronic Systems*, vol. 57, no. 1, pp. 485–496, 2021.

[24] W. Kong, J. Hong, M. Jia, J. Yao, W. Cong, H. Hu, and H. Zhang, "Yolov3-dpfin: A dual-path feature fusion neural network for robust real-time sonar target detection," *IEEE Sensors Journal*, vol. 20, no. 7, pp. 3745–3756, 2020.

[25] K. Wang, S. Li, S. Niu, and K. Zhang, "Detection of infrared small targets using feature fusion convolutional network," *IEEE Access*, vol. 7, pp. 146 081–146 092, 2019.

[26] Y. Dai, Y. Wu, F. Zhou, and K. Barnard, "Attentional local contrast networks for infrared small target detection," 2020.

[27] T. G. Kolda and B. Bader, "Tensor decompositions and applications," *Siam Review*, vol. 51, no. 3, pp. 455–500, 2009.

[28] J. Xue, Y. Zhao, S. Huang, W. Liao, J. C.-W. Chan, and S. G. Kong, "Multilayer sparsity-based tensor decomposition for low-rank tensor completion," *IEEE Transactions on Neural Networks and Learning Systems*, 2021.

[29] L. Grasedyck, "Hierarchical singular value decomposition of tensors," *SIAM Journal on Matrix Analysis and Applications*, vol. 31, no. 4, pp. 2029–2054, 2010.

[30] Y. Bu, Y. Zhao, J. Xue, J. C.-W. Chan, S. G. Kong, C. Yi, J. Wen, and B. Wang, "Hyperspectral and multispectral image fusion via graph laplacian-guided coupled tensor decomposition," *IEEE Transactions on Geoscience and Remote Sensing*, vol. 59, no. 1, pp. 648–662, 2020.

[31] H.-K. Liu, L. Zhang, and H. Huang, "Small target detection in infrared videos based on spatio-temporal tensor model," *IEEE Transactions on Geoscience and Remote Sensing*, vol. 58, no. 12, pp. 8689–8700, 2020.

[32] P. Zhang, L. Zhang, X. Wang, F. Shen, T. Pu, and C. Fei, "Edge and corner awareness-based spatial–temporal tensor model for infrared small-target detection," *IEEE Transactions on Geoscience and Remote Sensing*, vol. 59, no. 12, pp. 10 708–10 724, 2021.

[33] D. Pang, T. Shan, W. Li, P. Ma, S. Liu, and R. Tao, "Infrared dim and small target detection based on greedy bilateral factorization in image sequences," *IEEE Journal of Selected Topics in Applied Earth Observations and Remote Sensing*, vol. 13, pp. 3394–3408, 2020.

[34] I. Masaaki, M. Takanori, and H. Kohei, "On tensor train rank minimization: Statistical efficiency and scalable algorithm," 2017.

[35] Y. Liu, F. Shang, L. Jiao, J. Cheng, and H. Cheng, "Trace norm regularized candecomp/parafac decomposition with missing data," *IEEE Trans Cybern*, vol. 45, no. 11, pp. 2437–2448, 2015.

[36] L. Yuan, C. Li, D. P. Mandic, J. Cao, and Q. Zhao, "Tensor ring decomposition with rank minimization on latent space: An efficient approach for tensor completion," *CoRR*, vol. abs/1809.02288, 2018. [Online]. Available: http://arxiv.org/abs/1809.02288

[37] L. Zhang, L. Peng, T. Zhang, S. Cao, and Z. Peng, "Infrared small target detection via non-convex rank approximation minimization joint l2,1 norm," *Remote Sensing*, vol. 10, no. 11, 2018.

[38] X. Guan, L. Zhang, S. Huang, and Z. Peng, "Infrared small target detection via non-convex tensor rank surrogate joint local contrast energy," *Remote Sensing*, vol. 12, no. 9, p. 1520, 2020.

[39] H. J. A. M. Heijmans, "Composing morphological filters," *IEEE Transactions on Image Processing*, vol. 6, no. 5, pp. 713–723, 1997.

[40] J. Serra, "Image analysis and mathematical morphology," *Biometrics*, vol. 39, no. 2, p. 536, 1982.

[41] P. Maragos and R. W. Schafer, "Morphological filters–part ii: Their relations to median, order-statistic, and stack filters," *IEEE Transactions on Acoustics Speech and Signal Processing*, vol. 35, no. 8, pp. 1170–1184, 1987.

[42] Y. E. Bin and J. Peng, "Small target detection method based on morphology top-hat operator," *Journal of Image and Graphics*, vol. 7, no. 07, pp. 638–642, 2002.

[43] F. Zhang, C. Li, and L. Shi, "Detecting and tracking dim moving point target in ir image sequence," *Infrared Physics and Technology*, vol. 46, no. 4, pp. 323–328, 2005.

[44] P. T. Jackway, "Improved morphological top-hat," *Electronics Letters*, vol. 36, no. 14, pp. 1194–1195, 2002.

[45] L. Deng, J. Zhang, G. Xu, and H. Zhu, "Infrared small target detection via adaptive m-estimator ring top-hat transformation," *Pattern Recognition*, vol. 112, no. 1, p. 107729, 2020.

[46] J. Mira, A. E. Delgado, A.Fernandez-Caballero, and M. A. Fernandez, "Knowledge modelling for the motion detection task: The algorithmic lateral inhibition method," *Expert Systems with Applications*, vol. 27, no. 2, pp. 169–185, 2004.

[47] Y. Won, P. D. Gader, and P. C. Coffield, "Morphological shared-weight networks with applications to automatic target recognition," *IEEE Transactions on neural networks*, vol. 8, no. 5, pp. 1195–1203, 1997.

[48] X. Bai and F. Zhou, "Analysis of new top-hat transformation and the application for infrared dim small target detection," *Pattern Recognition*, vol. 43, no. 6, pp. 2145–2156, 2010.

[49] T. Lei, X. Jia, T. Liu, S. Liu, H. Meng, and A. K. Nandi, "Adaptive morphological reconstruction for seeded image segmentation," *IEEE Transactions on Image Processing*, vol. 28, no. 11, pp. 5510–5523, 2019.

[50] M. E. Kilmer, K. Braman, N. Hao, and R. C. Hoover, "Third-order tensors as operators on matrices: A theoretical and computational framework with applications in imaging," *SIAM Journal on Matrix Analysis and Applications*, vol. 34, no. 1, pp. 148–172, 2013.

[51] W. Wang, V. Aggarwal, and S. Aeron, "Efficient low rank tensor ring completion," in *2017 IEEE International Conference on Computer Vision (ICCV)*, 2017, pp. 5698–5706.

[52] L. Yuan, J. Cao, Q. Wu, and Q. Zhao, "Higher-dimension tensor completion via low-rank tensor ring decomposition," *CoRR*, vol. abs/1807.01589, 2018. [Online]. Available: http://arxiv.org/abs/1807.01589

[53] H. Huang, Y. Liu, Z. Long, and C. Zhu, "Robust low-rank tensor ring completion," *IEEE Transactions on Computational Imaging*, vol. 6, pp. 1117–1126, 2020.

[54] P. T. Jackway, "Improved morphological top-hat," *Electronics Letters*, vol. 36, no. 14, pp. 1194–1195, 2002.

[55] D. Wang, "A multiscale gradient algorithm for image segmentation using watersheds," *Pattern Recognition*, vol. 30, no. 12, pp. 2043–2052, 1997.

[56] M. S. Miri and A. Mahloojifar, "Retinal image analysis using curvelet transform and multistructure elements morphology by reconstruction," *IEEE Transactions on Biomedical Engineering*, vol. 58, no. 5, pp. 1183–1192, 2011.

[57] Y. Li, M. Xu, X. Liang, and W. Huang, "Application of bandwidth emd and adaptive multiscale morphology analysis for incipient fault diagnosis of rolling bearings," *IEEE Transactions on Industrial Electronics*, vol. 64, no. 8, pp. 6506–6517, 2017.

[58] P. Purkait and B. Chanda, "Super resolution image reconstruction through bregman iteration using morphologic regularization," *IEEE Transactions on Image Processing*, vol. 21, no. 9, pp. 4029–4039, 2012.

[59] C. Gao, D. Meng, Y. Yang, Y. Wang, X. Zhou, and A. G. Hauptmann, "Infrared patch-image model for small target detection in a single image," *IEEE Transactions on Image Processing*, vol. 22, no. 12, pp. 4996–5009, 2013.

[60] H. Zhang, L. Zhang, D. Yuan, and H. Chen, "Infrared small target detection based on local intensity and gradient properties," *Infrared Physics and Technology*, vol. 89, pp. 88–96, 2017.

[61] L. Zhang and Z. Peng, "Infrared small target detection based on partial sum of the tensor nuclear norm," *Remote Sensing*, vol. 11, no. 4, p. 382, 2019.

[62] H. Zhu, S. Liu, L. Deng, Y. Li, and F. Xiao, "Infrared small target detection via low-rank tensor completion with top-hat regularization," *IEEE Transactions on Geoscience and Remote Sensing*, vol. 58, no. 2, pp. 1004–1016, 2020.

[63] M. Nasiri and S. Chehresa, "Infrared small target enhancement based on variance difference," *Infrared Physics and Technology*, vol. 82, pp. 107–119, 2017.

Lizhen Deng (M'17) received the B.S. degree in electronic information science and technology from Huaibei Coal Industry Teachers College, Huaibei, China, in 2007, and the M.S. degree in communication and information systems from Nanjing University of Aeronautics and Astronautics, Nanjing, China, in 2010. She received her Ph.D. degree in electrical engineering from Huazhong University of Science and Technology, China, in 2014. In 2014, she joined the Nanjing University of Posts and Telecommunications, Nanjing, China. Her current research interests include image processing, computer vision, pattern recognition, and spectral data processing.

Guoxia Xu (M'19) received the B.S. degree in information and computer science from Yancheng Teachers University, Jiangsu Yancheng, China in 2015, and the M.S. degree in computer science and technology from Hohai University, Nanjing, China in 2018. Now, he is pursing his Ph.D. degree in Department of Computer Science, Norwegian University of Science and Technology, Gjovik Norway. His research interest includes pattern recognition, image processing, and computer vision.

Jie Song is currently pursuing the B.S. degree in electronic information engineering with the Nanjing University of Posts and Telecommunications, Nanjing, China. His research interest includes computer vision and image processing.

Hu Zhu (M'17) received the B.S. degree in mathematics and applied mathematics from Huaibei Coal Industry Teachers College, Huaibei, China, in 2007, and the M.S. and Ph.D. degrees in computational mathematics and pattern recognition and intelligent systems from Huazhong University of Science and Technology, Wuhan, China, in 2009 and 2013, respectively. In 2013, he joined the Nanjing University of Posts and Telecommunications, Nanjing, China. His research interests include pattern recognition, image processing, and computer vision.